

Article

Tailoring Magnetic and Transport Anisotropies in $\text{Co}_{100-x}\text{-Cu}_x$ Thin Films through Obliquely Grown Nano-Sheets

Cristina Favieres^{1,2,*}, José Vergara^{1,2} and Vicente Madurga¹

¹ Laboratory of Magnetism, Department of Science (Physics), Public University of Navarre (UPNA), Campus de Arrosadía, 31006 Pamplona, Spain; jvergara@unavarra.es (J.V.); vmadurga@unavarra.es (V.M.)

² Institute for Advanced Materials and Mathematics (INAMAT2), Public University of Navarre (UPNA), Campus de Arrosadía, 31006 Pamplona, Spain

* Correspondence: favieresc@unavarra.es

Abstract: The magnetic and transport properties of pulsed laser-deposited $\text{Co}_{100-x}\text{-Cu}_x$ thin films were tailored through their nano-morphology and composition by controlling for the deposition geometry, namely normal or oblique deposition, and their Cu content. All films were composed of an amorphous Co matrix and a textured growth of Cu nanocrystals, whose presence and size d increased as x increased. For $x = 50$, all films were superparamagnetic, regardless of deposition geometry. The normally deposited films showed no in-plane magnetic anisotropy. On the contrary, controllable in-plane uniaxial magnetic anisotropy in both direction and magnitude was generated in the obliquely deposited films. The magnetic anisotropy field H_k remained constant for $x = 0, 5$ and 10 , $H_k \approx 35 \text{ kAm}^{-1}$, and decreased to 28 and 26 kAm^{-1} for $x = 20$ and 30 , respectively. This anisotropy had a magnetostatic origin due to a tilted nano-sheet morphology. In the normally deposited films, the coercive field H_c increased when x increased, from 200 ($x = 0$) to 1100 Am^{-1} ($x = 30$). In contrast, in obliquely deposited films, H_c decreased from 1500 ($x = 0$) to 100 Am^{-1} ($x = 30$) as x increased. Activation energy spectra corresponding to structural relaxation phenomena in obliquely deposited films were obtained from transport property measurements. They revealed two peaks, which also depended on their nano-morphology and composition.

Keywords: magnetic thin films; nano-morphology; magnetic anisotropy; transport properties; structural relaxation; activation energy spectra; pulsed laser deposition; Scanning Tunneling Microscopy (STM)



Citation: Favieres, C.; Vergara, J.; Madurga, V. Tailoring Magnetic and Transport Anisotropies in $\text{Co}_{100-x}\text{-Cu}_x$ Thin Films through Obliquely Grown Nano-Sheets. *Magnetochemistry* **2022**, *8*, 4. <https://doi.org/10.3390/magnetochemistry8010004>

Academic Editor: David S. Schmol

Received: 2 December 2021

Accepted: 23 December 2021

Published: 28 December 2021

Publisher's Note: MDPI stays neutral with regard to jurisdictional claims in published maps and institutional affiliations.



Copyright: © 2021 by the authors. Licensee MDPI, Basel, Switzerland. This article is an open access article distributed under the terms and conditions of the Creative Commons Attribution (CC BY) license (<https://creativecommons.org/licenses/by/4.0/>).

1. Introduction

Magnetic thin films are extensively studied owing to their suitability for numerous scientific and technological devices [1–4]. These films have a broad range of applications in ultra-high frequency devices, data storage, write-read heads, and in microelectromechanical systems, such as sensors, actuators, micromotors, etc. [5–7]. In particular, the control of the magnetic properties of thin films via the deposition techniques allows for the optimization of these applications. Certainly, the nano-structure, nano-morphology, films composition, use of buffer or capping layers, etc. can be precisely tailored during the growth, thus influencing the magnetic behavior [8–12]. Among these techniques, physical vapor deposition ones are extensively used [13–16]. In particular, using the Pulsed Laser Deposition (PLD) technique, we fabricated ferromagnetic Co and Co-rich thin films with a distinctive and particular nano-morphology observed by HRTEM: They are formed by tilted nano-sheets, whose dimensions are between ≈ 2.5 and 5 nm thick, between ≈ 30 – 100 nm wide and ≈ 200 – 300 nm long, with an inter-sheet distance of ≈ 1 – 2 nm and tilted ≈ 55 – 60 deg. with respect to the film plane, values that depend on the element accompanying the Co [17–19]. This special nano-morphology confers them numerous anisotropic physical properties such as magnetic, electrical, transport, optical and mechanical properties [17–23].

Ferromagnetic Co–Cu materials are widely used due to their interesting magnetic and transport properties; these properties are affected by the shape and nanostructure of the materials (among other parameters) and can be controlled by deposition techniques [24–32] (and references therein). These Co–Cu materials are known to be suitable for devices used, for example, in microelectronics and telecommunication [6], ultra-high energy storage systems [33], spintronics applications [34], magneto-resistive sensors [35,36] or catalytic applications [37,38].

In this work, we present the magnetic properties of Co-rich PLD Co–Cu thin films. We shall show the influence in their magnetic and transport behavior of (i) the deposition parameters, specifically the angle of incidence during deposition, i.e., normal deposition or oblique deposition and (ii) the Cu content. The values of the in-plane uniaxial magnetic anisotropy field, coercive field and magnetization processes, as well as the activation energy spectra corresponding to the temperature-induced structural relaxation processes—linked to their nano-structure and nano-morphology and composition—will be analyzed and discussed.

2. Experimental Procedures

Thin films of Co–Cu were grown in a PLD stainless-steel chamber at a base pressure of 10^{-6} mbar. A pulsed Nd–YAG laser with $\lambda = 1064$ nm, 20 Hz repetition rate, 6 ns pulse and an energy of 200 mJ/pulse in the target's spot, ≈ 6 mm² in area, laser fluence 3.3 J/cm², was introduced into the chamber through a quartz window. The angle of incidence of the laser beam on the target was 45 degrees. We fabricated a circular target, 25 mm in diameter, formed by two circular sectors of Co and Cu, both 99.9% pure. We labeled the films as Co_{100-x}–Cu_x where x is the area of the Cu sector with respect to the total area of the target, varying as $x = 0, 5, 10, 20, 30$ and 50. This target always rotated at 32 rpm. Based on our previous works, a target revolving 32 turns per min ensured that the target composition transferred sufficiently well to the deposited films. It is also known that stoichiometry can be preserved in PLD processes by controlling for parameters such as, e.g., laser fluence, substrate temperature, background gas pressure [13,39]. In these Co–Cu samples, the dispersion of Cu in Co was confirmed by the experimental results that will be shown below. Before each deposition, the target was mechanically polished with carbide grinding paper to always initiate the ablation–deposition under the same conditions, since the surface of the target influences the morphological and structural properties of the films [13,40]. The election of 32 rpm also ensured that no damage of the target surface occurred that could significantly affect the properties of the samples studied in this work. The target-to-substrate distance was 62 mm. The substrates were glass discs, 7 mm in diameter, 0.12 mm in thickness, and rectangular pieces of monocrystalline (111) Si $\approx 20 \times 8$ mm² in area and 450 μ m in thickness. All of them were cleaned in pure methanol prior to the deposition.

A detailed description on the relative arrangement and spatial symmetries of the laser beam, the target and the substrates for the oblique deposition can be found in Reference [17]. The substrates were placed along the generatrix of a cone, allowing for deposition at an oblique angle of incidence $\theta_i = 55$ deg. (see Figure 1). For a deposition time of 30 min, the thickness of the pure Co films was (80 ± 10) nm, as we determined by atomic force microscopy. Simultaneously, other substrates were placed in the cone but at an angle $\theta_i = 0$ deg., that is, for normal deposition. During deposition, a custom-made system permitted the substrate holder to rotate at 72 rpm with respect to its symmetry axis, which allowed for the production of highly homogeneous samples. A thickness of (140 ± 10) nm corresponded to these Co normally deposited films.

The surface nano-morphology of the samples was studied by Scanning Tunneling Microscopy (STM) and the images have been adapted using a Nanotec software [41].

The structure of the samples was investigated by X-ray diffraction (XRD) in the grazing incidence mode (angle 1.0°), with Cu K α radiation operating at 40 kV and 35 mA and a scan step of 0.1°. The background signals corresponding to the Si substrate were subtracted from all of the spectra.

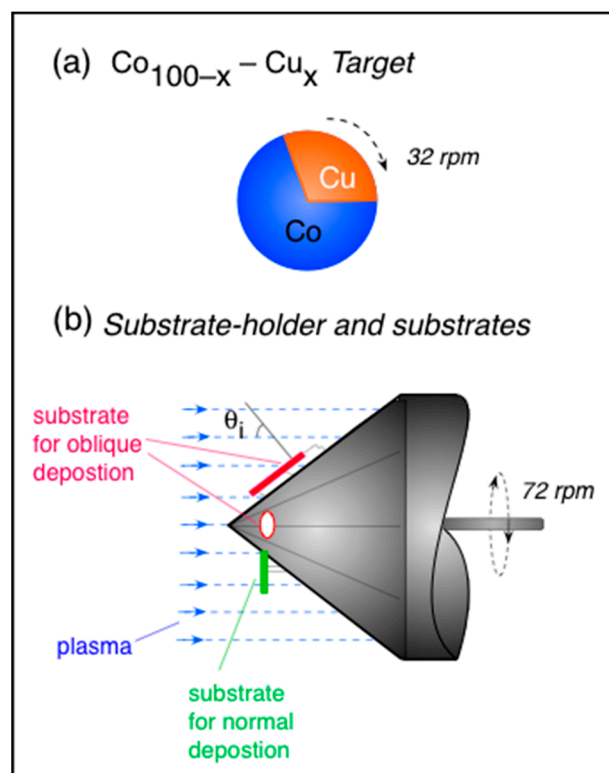


Figure 1. Schematic drawing. (a) Top view of the $\text{Co}_{100-x}\text{-Cu}_x$ target formed by two circular sectors, one of Co and one of Cu. x is the Cu sector area with respect to the total area of the target. The target rotated at 32 rpm. x was varied at 0, 5, 10, 20, 30 and 50. (b) Substrate holder and substrates: Substrates of glass and Si (111) were placed in the generatrix of the substrate holder (cone), allowing for deposition at an oblique angle of incidence $\theta_i = 55$ deg. Simultaneously, substrates were placed in the cone at $\theta_i = 0$ deg. for normal deposition. The cone rotated at 72 rpm.

The films were magnetically characterized by measuring the M – H hysteresis loops at room temperature with a Vibrating Sample Magnetometer (VSM). The magnetic field was applied in the plane of the films. By rotating the film in the magnetic field around the normal of its plane, it was possible to find the in-plane easy and hard directions of magnetization. The magnetic anisotropy field, H_k ($H_k = 2k/\mu_0 M_s$, with k as the anisotropy constant and $\mu_0 M_s$ as the saturation magnetization), was determined from the crossover of the hard loop. The samples were also magnetically characterized by measuring their hysteresis loops with the magnetic field applied perpendicularly to their plane.

Magneto-optical M – H hysteresis loops were measured by means of the Transversal Magneto-optical Kerr Effect (MOKE). The AC magnetic field (77 Hz) was created with two Helmholtz coils. The magnetic field was applied in the plane of the films. A home-built system permitted the rotation of the samples around an axis perpendicular to their plane, allowing to find the in-plane easy and hard directions for the magnetization.

The samples were annealed at 270 °C in a dynamic Ar atmosphere. Once the films reached this temperature, they were removed from the hot region of the furnace. Their M – H loops were then measured at room temperature. This temperature was chosen because knowing that the Co films lost their magnetic anisotropy after being heated at this temperature [18], one of our aims for the present work was investigating the possible influence of Cu content in that behavior.

The dependence of the electrical resistance R of the samples on temperature, from room temperature to 450 °C, was measured in a home-made system placed inside a furnace. To avoid oxidation phenomena, the films were kept in a dynamic inert Ar atmosphere during the whole process. The heating rate was 10 °C·min^{−1}. $R(T)$ was measured between two contacts separated by 4.5 mm.

3. Results and Discussion

3.1. $\text{Co}_{100-x}\text{-Cu}_x$ Obtained by Normal Deposition: Structure and Magnetic Properties

We first present the results obtained for the normally deposited samples, from now on labeled as 0 deg. films.

With regard to their structure, we refer to the XRD measurements shown in Figure 2.

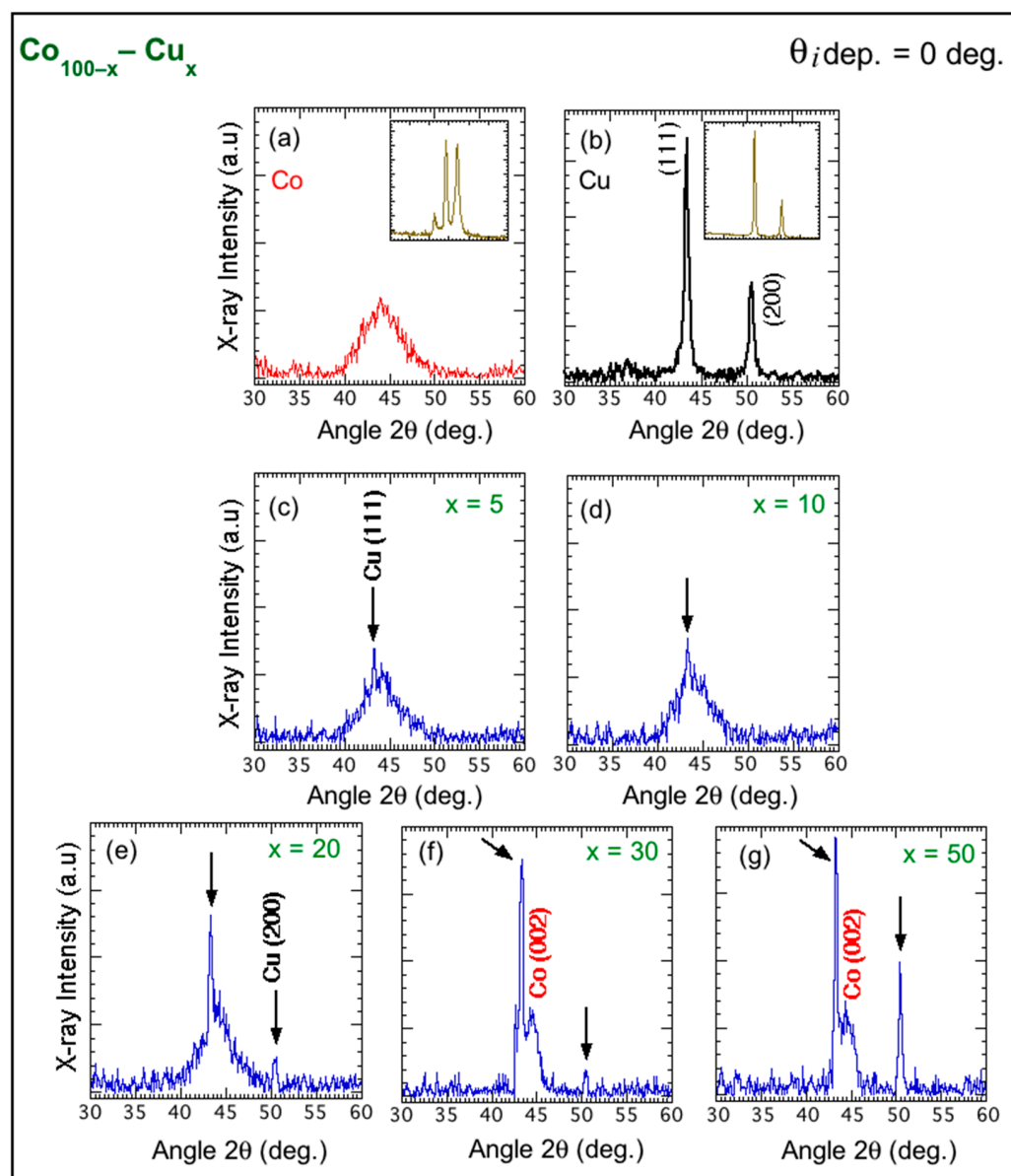


Figure 2. (a–g) XRD measurements of normally deposited $\text{Co}_{100-x}\text{-Cu}_x$ thin films, including those of pure Co and pure Cu films. x is the proportion of Cu on the target surface. The insets in (a,b) show the spectra corresponding to the Co and Cu crystalline targets used for the deposition. The peaks corresponding to the Co (100), Co (002) and Co (101) (in increasing order of the Bragg angle) are visualized in the (a) inset and those of Cu (111) and Cu (002) are visible in (b) inset. (c–g) The crystalline Cu peaks detected in the films with $x = 5, 10, 20, 30$ and 50 are indexed and marked with a black arrow, ($\theta_{\text{deposition}} = 0$ deg.).

The Co film, Figure 2a, displayed the characteristic halo of an amorphous or nano-crystalline material. We used the Scherrer's formula [42] to estimate the average size of the nano-crystallites, $d = 0.9\lambda/B\cos\theta$, with λ as the wavelength of the X-ray beam, B as the line broadening at half the maximum intensity and θ as the Bragg angle. We calculated

$d \approx 1.2$ nm for Co nano-crystallites, which is in accordance with our previous studies (by transmission electron microscopy) of similar Co samples [43]. On the contrary, the pure Cu film spectrum, Figure 2b, revealed some correspondence with the crystalline nature of the target: The two principal peaks corresponding to diffraction from the Cu (111) and (200) planes of the fcc structure were present, although slightly shifted (0.2 deg.) to smaller diffraction angles. This could be indicative of small residual strains in the samples. Scherrer's formula gave a value of $d \approx 11.4$ nm for the Cu (111) crystallites, which produced the most intense peak.

For $x = 5$, it was observed that the crystalline peak corresponded to the Cu (111) planes; moreover, its intensity increased notably as the Cu content increased (Figure 2c–g). There was also a progressive increase in the peak intensity of the (200) planes as Cu was incorporated in the Co matrix, but this peak was less intense than that corresponding to the (111) peak, observing a texture in the Cu growth. Estimation of the size of the Cu grains corresponding to the (111) planes gave $d \approx 7.9$ nm for $x = 5$, $d \approx 11.8$ nm for $x = 10$, $d \approx 15.3$ nm for $x = 20$, $d \approx 18.8$ nm for $x = 30$, and for $x = 50$, $d \approx 22.5$ nm. These data confirmed that in $\text{Co}_{100-x}\text{-Cu}_x$ films, Cu nano-crystallites grew more easily than those of Co. It was already noted above that pure Co films grew amorphous, while pure Cu films exhibited crystalline peaks, see Figure 2a,b. Thus, in agreement with what was expected from the deposition of the samples, a dispersion of nano-crystallites of Cu was found in the Co matrix, whose proportion and size increased as the concentration of Cu in the target (and hence in the films) increased.

Figure 3 shows the in-plane hysteresis loops corresponding to these samples.

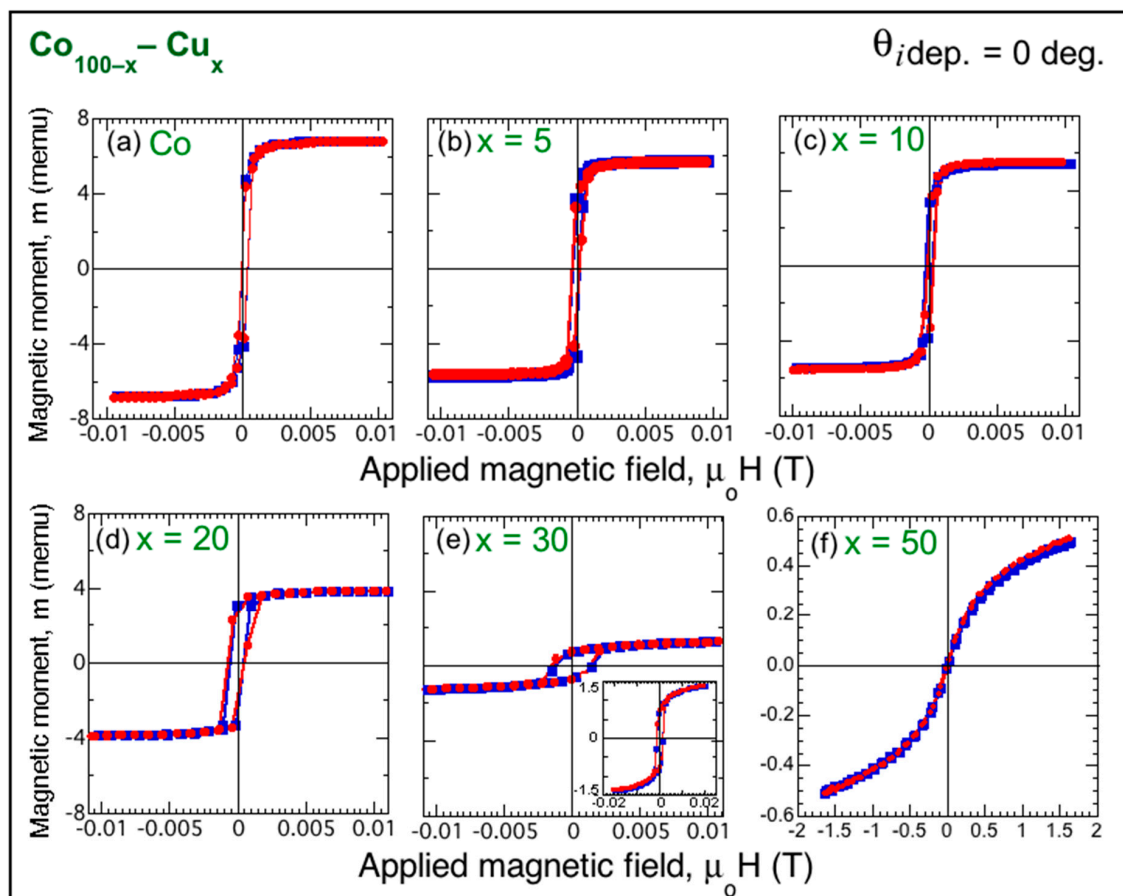


Figure 3. (a–f) VSM in-plane hysteresis loops corresponding to normally deposited $\text{Co}_{100-x}\text{-Cu}_x$ films, magnetized into two mutually perpendicular directions. x is the proportion of Cu on the target surface. The solid lines are visual guides. (f) Note the different loops of the sample with $x = 50$ and the different scales in both, m and $\mu_0 H$, ($\theta_{\text{ideposition}} = 0$ deg.).

From these M - H loops, their in-plane isotropic magnetic behavior was deduced. Those corresponding to $x = 0, 5, 10$ and 20 were soft magnetically, with high magnetic susceptibility, high remanence and low coercive fields, H_c . This increased from $H_c = 200 \text{ Am}^{-1}$ for Co to $H_c = 400 \text{ Am}^{-1}$ for $x = 20$. Moreover, these facts were observed: For $x = 30$, the magnetic saturation was not reached as easily as for the samples with lower Cu content (see inset in Figure 3e); the ratio remanent magnetic moment/maximum magnetic moment m_r/m_{\max} was only ≈ 0.50 , while for the other samples, it was between ≈ 0.7 – 0.8 . H_c corresponding to this sample increased significantly with respect to the other ones: $H_c = 1110 \text{ Am}^{-1}$ for $x = 30$. In addition, the film corresponding to $x = 50$, Figure 3f, displayed a completely different behavior, superparamagnetic-like [44]. This film was not magnetically saturated in an applied magnetic field of 1.7 T and both the remanence and the coercive field were zero.

The soft magnetic behavior of these films was corroborated by MOKE measurements. Figure 4a,b shows some MOKE loops of the $x = 0, 5, 20$ and 30 samples. The film corresponding to $x = 30$ was not as soft as the other ones, which also confirmed the behavior shown in the VSM loops. Figure 4c shows the dependence of H_c with x . These values were obtained from these MOKE loops, and they were similar to those corresponding to the VSM loops. Noteworthy, H_c increased with x , especially for $x = 20$ and 30 , which was coincident with the increase of the size d of the Cu grains, especially for those corresponding to the Cu (111) planes deduced from Figure 2. Figure 4d shows dependence of H_c with d .

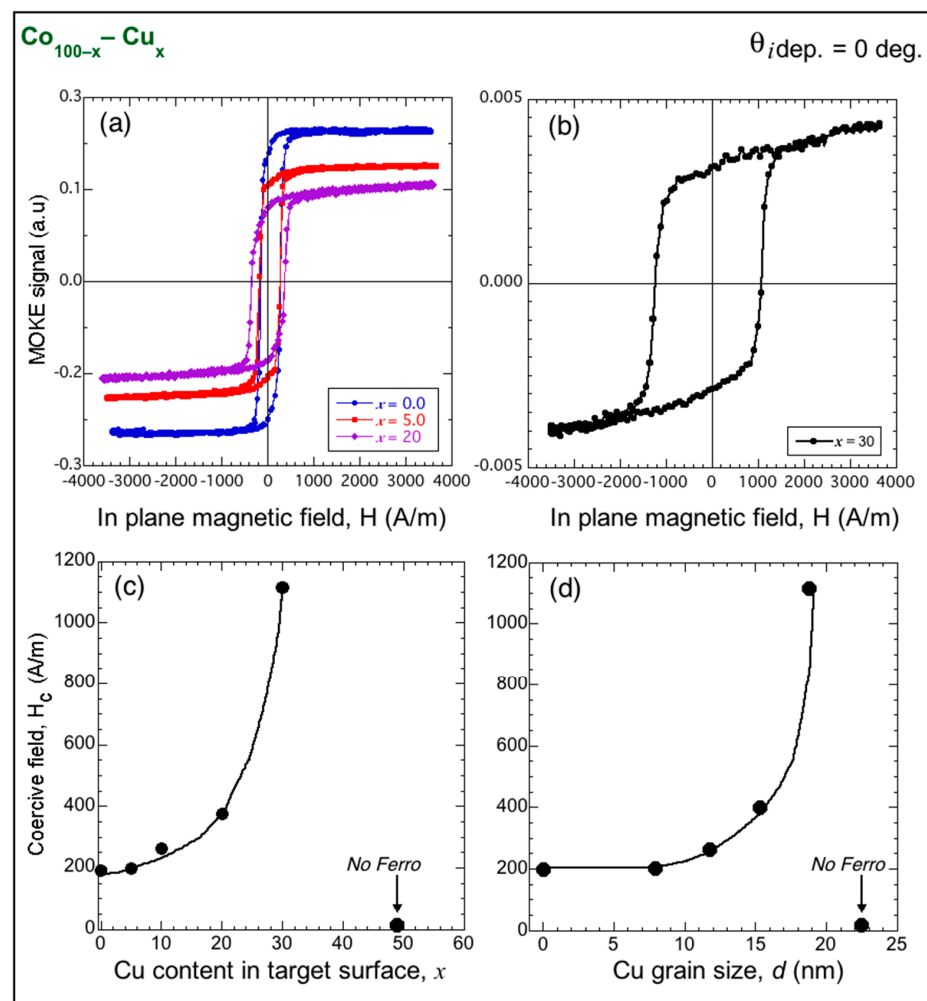


Figure 4. MOKE loops of $\text{Co}_{100-x}\text{-Cu}_x$ normally deposited films (a) $x = 0, 5$, and 20 . (b) $x = 30$. x is the proportion of Cu on the target surface. (c) Evolution of the coercive field H_c with x . (d) Dependence of H_c with the average size of the Cu grains that correspond mainly to Cu (111). The $x = 50$ film ($d = 22.5 \text{ nm}$) is shown as non-ferromagnetic. The lines are visual guides, ($\theta_{\text{deposition}} = 0 \text{ deg.}$).

The values of the spontaneous magnetization $\mu_0 M_s$ of each sample were deduced by measuring the saturation magnetic field when applying the field in the direction perpendicular to the plane of the films [45]. Figure 5a,b shows the measurements corresponding to the $x = 0$ and $x = 50$ films, respectively. It is seen that the Co film was saturated for a field ≈ 1.4 T; meanwhile, the $x = 50$ film did not reach saturation even for an applied field of 1.8 T, confirming its superparamagnetic-like behavior. Figure 5c shows the values of $\mu_0 M_s$ measured for all of the $\text{Co}_{100-x}\text{-Cu}_x$ films. An almost linear dependence of $\mu_0 M_s$ with the Cu content could be assumed. The values of the maximum magnetic moment measured by applying a magnetic field of 0.01 T in the plane of the films are also plotted in Figure 5.

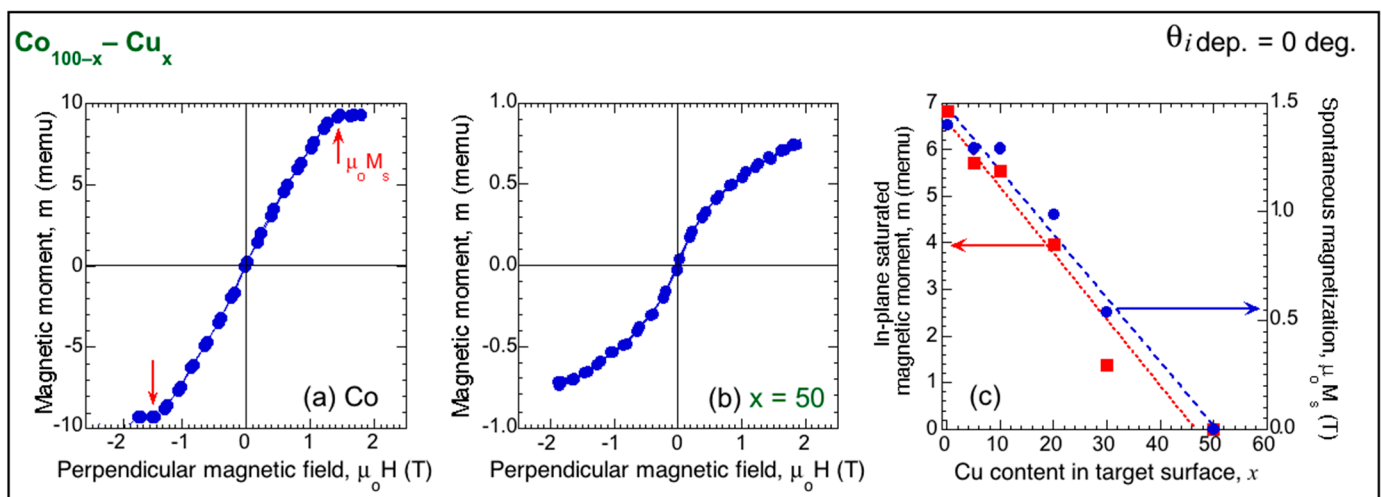


Figure 5. M - H loops corresponding to $\text{Co}_{100-x}\text{-Cu}_x$ normally deposited films. The loops were obtained by applying the magnetic field in the direction perpendicular to the plane of the films. (a) $x = 0$, pure Co; (b) $x = 50$, with a superparamagnetic behavior. Note the different values in the magnetic moment scale in (a,b). x is the proportion of Cu on the target surface. (c) Evolution with x of the saturated in-plane magnetic moment measured by applying a magnetic field of 0.01 T and evolution of the spontaneous magnetization $\mu_0 M_s$ with x measured by applying the magnetic field perpendicularly to the plane of the films. The dotted lines are visual guides, ($\theta_{i\text{deposition}} = 0 \text{ deg.}$).

3.2. $\text{Co}_{100-x}\text{-Cu}_x$ Obtained by Oblique Deposition: Structure, Nano-Morphology, Magnetic and Transport Properties

Figure 6 shows the XRD spectra of obliquely deposited $\text{Co}_{100-x}\text{-Cu}_x$, from now on labeled as 55 deg. films, including those of pure Co and pure Cu thin films. From the point of view of the X-ray measurements, the 55 deg. Co sample was similar to the 0 deg. Co sample, since both presented the characteristic broad halo of an amorphous-like material. This agreed with our previous results [17,18]. The two principal peaks corresponding to the Bragg angle of Cu (111) and Cu (200) planes were seen in the Cu film spectrum, similar also to the 55 deg. sample, which, although noteworthy, the calculated value here for the Cu (111) crystallites was ≈ 9.5 nm, smaller than 11.4 nm, which was found for the 0 deg. Cu film.

The $\text{Co}_{100-x}\text{-Cu}_x$ film with $x = 5$ was amorphous or nano-crystalline, similar to that of Co, see Figure 6c. When x increased to $x = 10, 20, 30$ and 50 , traces of Cu crystallites were observed, see Figure 6d–g. Especially for the $x = 20, 30$ and 50 samples, the peaks corresponding to the Bragg angles from the (111) and (200) planes were well visible. For the $x = 20$ sample, the estimated size of the Cu (111) crystallites was $d \approx 5.7$ nm, increasing to ≈ 10.7 nm for the $x = 30$ sample and to ≈ 17.1 nm for the $x = 50$ film. Therefore, as x increased from $x = 20$ to 30 and to 50 , the average size of d increased markedly. In these samples, texture could also be inferred, as the (111) peak was more intense than the (200) one, as in the case of the pure Cu film. In all of the Co–Cu films in which the peaks were

detectable, the small shift (≈ 0.1 deg.) toward smaller diffraction angles (with respect to the corresponding Bragg angle of the Cu (111) planes) could also indicate slight tensile strains during deposition.

Comparing this with the results of Figure 2, we first deduced that the growth of larger grains of Cu, and even their growth in samples with a smaller proportion of Cu ($x = 5$ and $x = 10$), was easier in the 0 deg. films.

Figure 7 shows the surface nano-morphology corresponding to the obliquely deposited $\text{Co}_{100-x}\text{-Cu}_x$ sample with $x = 30$. In this Figure, the STM image corresponding to the normally deposited sample with $x = 30$, that is, $\theta_i = 0$ deg., has been included for comparison. It is seen in Figure 7d that the surface of the obliquely deposited film showed structures like nano-strings oriented perpendicular to the incidence plane of the plasma during deposition. This nano-morphology must correspond to the surface of nano-sheets, in accordance with our previous studies on pure Co [17,20,21] and on Co-V and Co-Zn films [19]. On the other hand, for normally deposited samples, see Figure 7a, there are no surface nano-strings (nor inner nano-sheets) but a random distribution of grains, also in agreement with our previous works on pure Co films [19,20].

In previous works [17–23], we showed that PLD Co and Co-rich thin films obtained at oblique incidence exhibited a well-defined in-plane uniaxial magnetic anisotropy, UMA, the origin of which we found to be magnetostatic because of their special morphology of oblique nano-sheets [17]. In the present work, we next show that these obliquely deposited Co-Cu films also displayed a clear UMA, see Figure 8, the easy direction of magnetization being perpendicular to the incidence plane of the plasma during deposition. We measured the magnetic anisotropy field, H_k , from the hard loops, hard loops without hysteresis, with zero remanence and zero coercive field.

The 55 deg. Co-Cu samples displayed different magnetic properties with respect to those of 0 deg. films. First, note the different scale of the applied magnetic field with respect to that shown in Figure 3 (corresponding to the 0 deg. films). The only property in common between the 55 deg. samples and the 0 deg. samples was the decrease from the beginning ($x = 5$) of the magnetic moment (and the saturation magnetization) as x increased.

From the results of the magnetic anisotropy shown in Figure 8, we can deduce that these Co-Cu samples were also formed by tilted nano-sheets in the same way as pure Co and Co-MT (MT = V, Zn . . .) films [17–19], since all of them were grown using the same set-up and configuration, and all of them exhibited the same uniaxial magnetic anisotropy (perpendicular to the incidence plane of the plasma during deposition). The results of Figure 8 revealed that the UMA was controlled, in value and direction, during the growth of the Co-Cu films; we found a decrease of $\approx 23\%$ in the value of H_k with the Cu content from $x = 5$ to $x = 30$, but it always maintained the same direction of the UMA.

The coercive field H_c measured in the easy direction decreased as x increased, from $H_c = 1500 \text{ Am}^{-1}$ ($x = 0$) to $H_c = 100 \text{ Am}^{-1}$ ($x = 30$). These values of H_c were notably lower than those of the anisotropy field H_k since the magnetization processes in the easy direction corresponded to nucleation and displacements of magnetic walls, as we know from our previous observation of the micro-structures of magnetic domains of similar Co PLD films [20,45–47]. This dependence of H_c with x was opposite to that found for the 0 deg. samples for which H_c increased with x .

Figure 9 shows the dependence of H_k with x (bearing in mind that the superparamagnetic sample $x = 50$ sample showed almost no magnetization and no UMA).

Figure 10a shows the MOKE loops (measured in the magnetization in-plane easy direction).

These MOKE loops confirmed the initial magnetization process by nucleation and displacements of magnetic domain walls, and they also confirmed that the values of H_c were similar in the two measurements, MOKE and VSM. These values are shown in Figure 10b as a function of x . Figure 10c shows the evolution of H_c with the size of the Cu nano-crystals. We assumed that both those corresponding to Cu (111) and Cu (200) were almost zero for $x = 0, 5$ and 10 , since in Figure 6, the peak detected with our diffractometer

was small, corresponding to the Cu (200) planes in the sample $x = 10$. We deduced that the average size of the nano-crystals should be around 1–2 nm.

The samples were annealed at 270 °C. As occurred in the pure Co samples [18], the Co–Cu films underwent a remarkable modification in their magnetic properties. Figure 11 shows the M – H loops of some of them. Compared with Figure 8, it is seen that the UMA disappeared after the heat-treatment and all of the samples became magnetically isotropic in the plane (samples with $x = 10$ and 30 are not shown here).

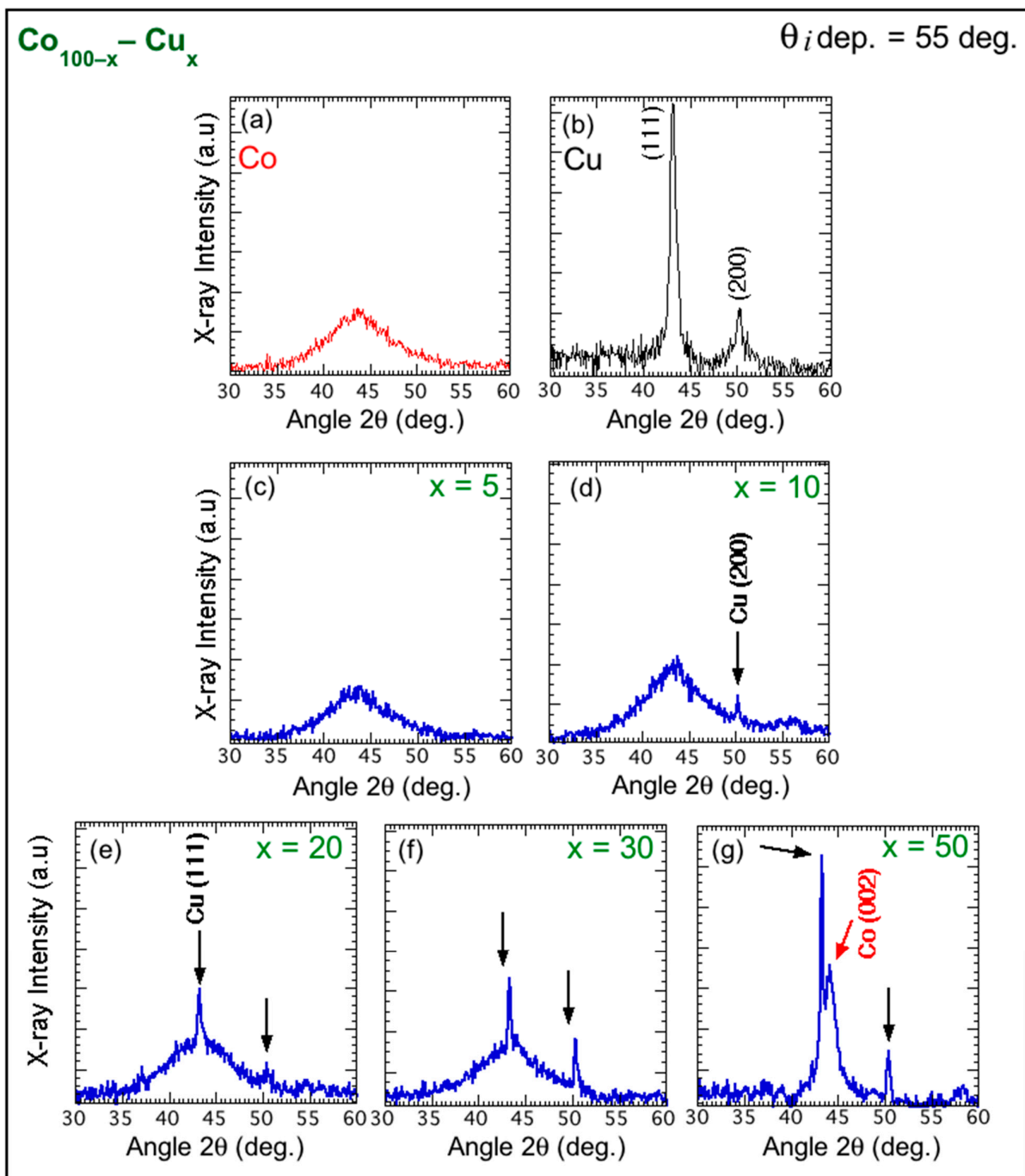


Figure 6. (a–g) XRD measurements of 55 deg. $\text{Co}_{100-x}\text{Cu}_x$ thin films corresponding to different x . x is the proportion of Cu on the target surface. There are included those of pure Co and pure Cu films. The peaks corresponding to crystalline Cu in the $\text{Co}_{100-x}\text{Cu}_x$ films with $x = 10, 20, 30$ and 50 are also indexed and marked with a black arrow, ($\theta_{\text{deposition}} = 55$ deg.).

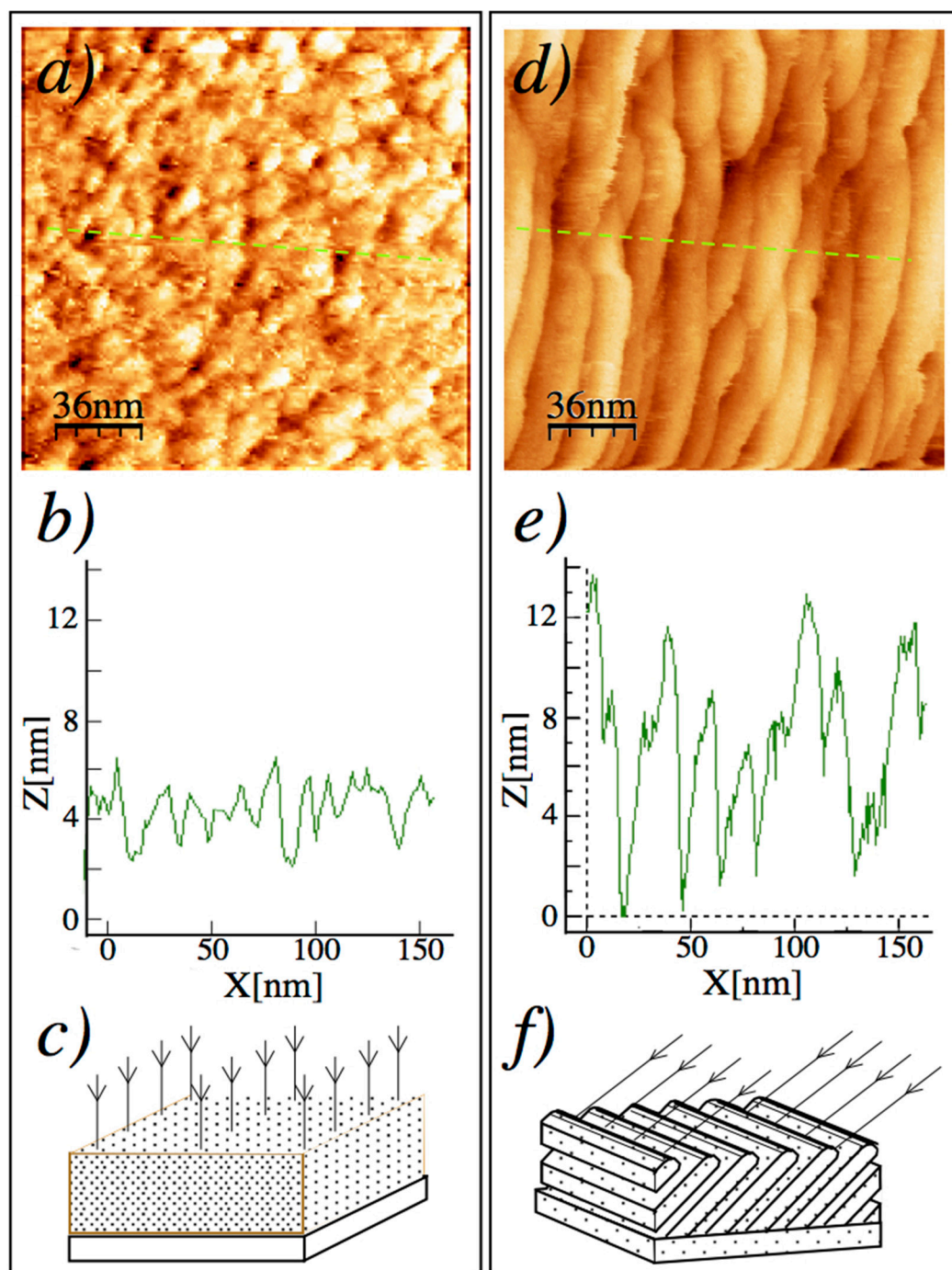


Figure 7. Surface topography corresponding to $\text{Co}_{100-x}\text{-Cu}_x$ samples. x is the proportion of Cu on the target surface. $x = 30$. (a–c) For normally deposited film, $\theta_{\text{deposition}} = 0$ deg.: (a) STM image. (b) Cross-sectional profile of this surface and (c) schematic drawing of the film, including the plasma direction (arrows). No nano-sheets are formed. (d–f) For obliquely deposited film, $\theta_{\text{deposition}} = 55$ deg.: (d) STM image of the surface. (e) Cross-sectional profile of this surface and (f) schematic drawing of the film and the plasma direction. Tilted nano-sheets are formed, whose top surfaces are revealed by STM.

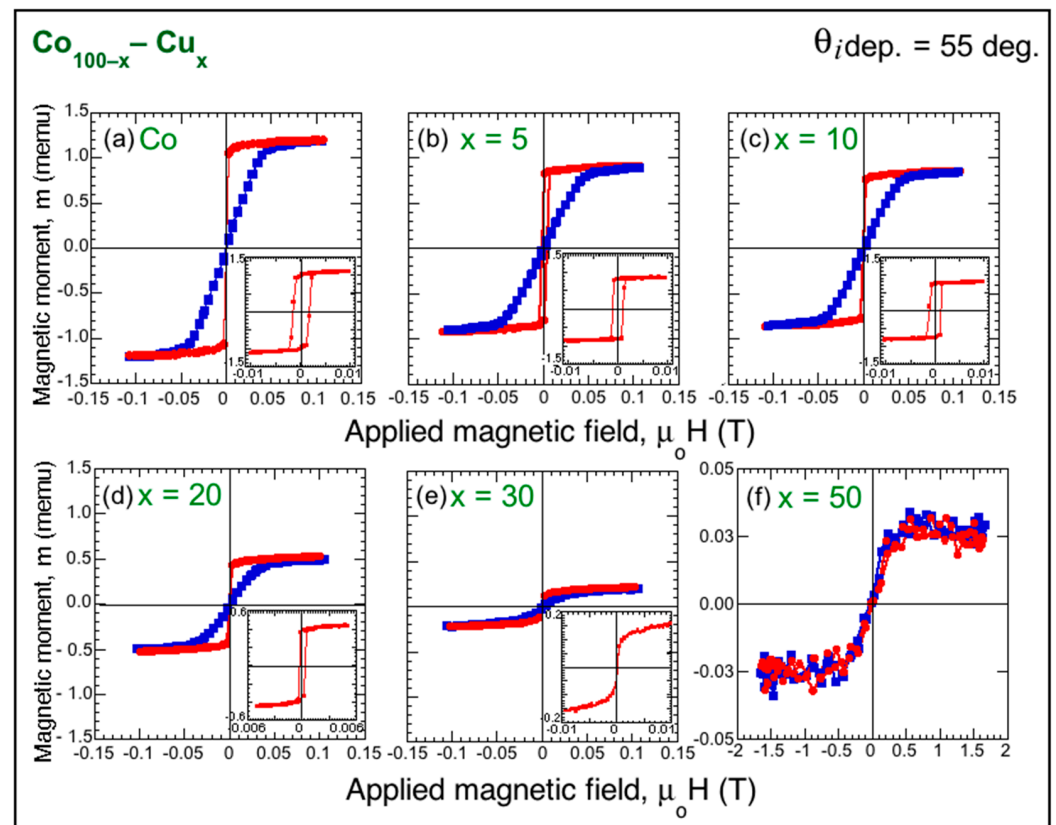


Figure 8. (a–f) VSM in-plane hysteresis loops corresponding to $\text{Co}_{100-x}\text{-Cu}_x$ series films with different x . x is the proportion of Cu on the target surface. Hard direction for the magnetization—blue square symbols; easy direction—red circle symbols. The solid lines are visual guides. The insets show magnification of the loops in the easy direction. (f) $x = 50$. Note here, the different behavior and the different scales on both the magnetic moment and applied magnetic field axes compared to the other samples, ($\theta_{i\text{deposition}} = 55$ deg.).

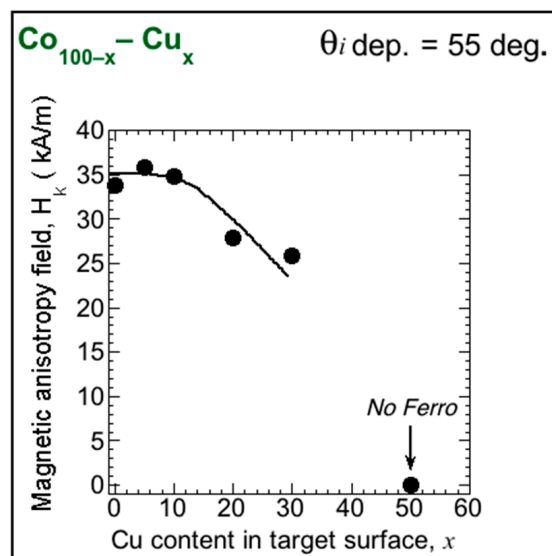


Figure 9. Dependence of the in-plane uniaxial magnetic anisotropy field H_k with x corresponding to $\text{Co}_{100-x}\text{-Cu}_x$ obliquely deposited films. x is the proportion of Cu on the target surface. The line is a visual guide. For $x = 50$, the samples are non-ferromagnetic, ($\theta_{i\text{deposition}} = 55$ deg.).

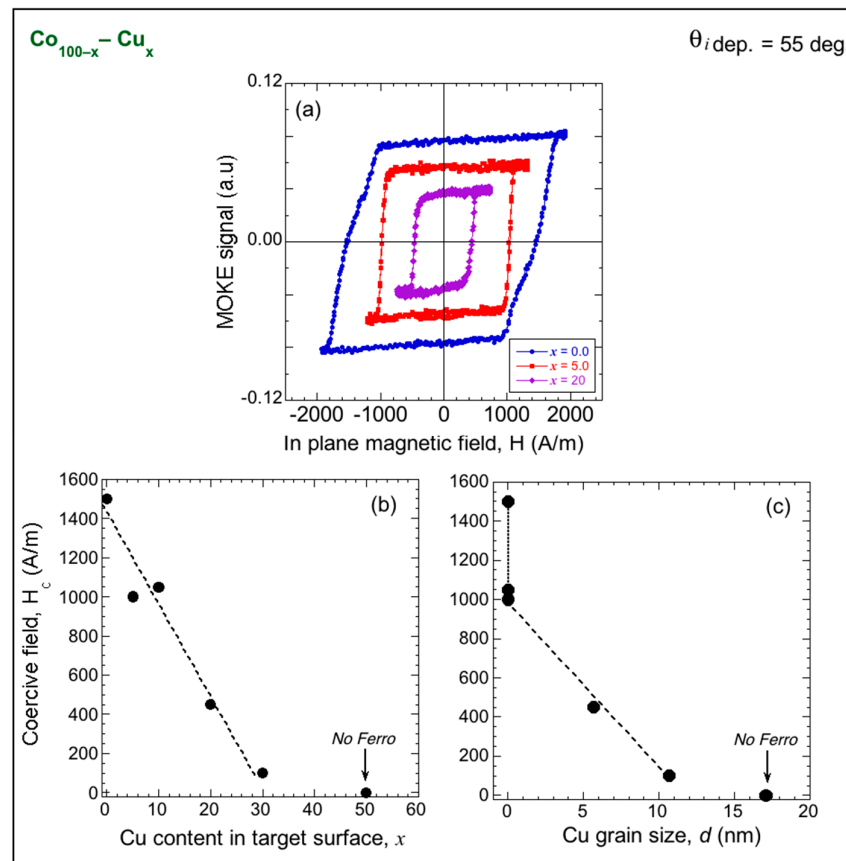


Figure 10. (a) MOKE loops, measured in the magnetization easy direction, corresponding to $\text{Co}_{100-x}\text{-Cu}_x$ films with $x = 0, 5$ and 20 . x is the proportion of Cu on the target surface. (b) Evolution of the coercive field H_c with x . (c) Dependence of H_c with the average size of the Cu (111) grains. See text for an explanation. The lines are visual guides. For $x = 50$, the samples are non-ferromagnetic, ($\theta_{\text{deposition}} = 55$ deg.).

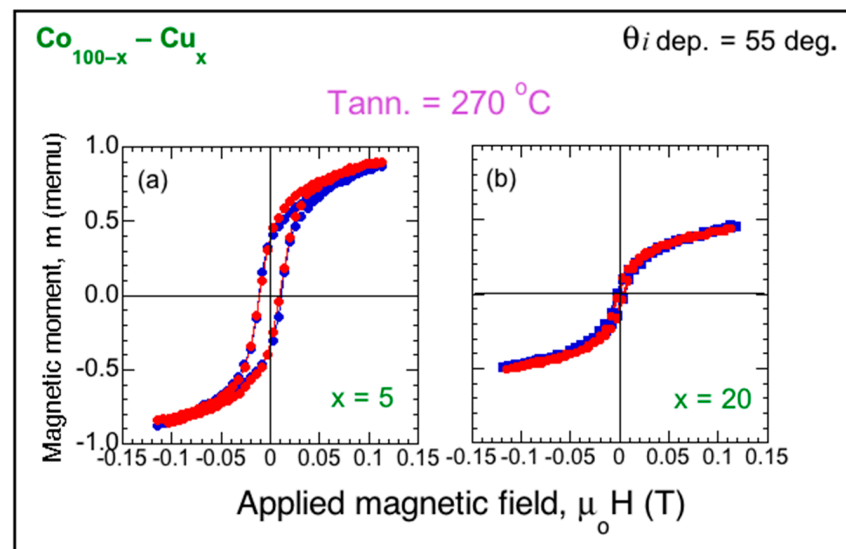


Figure 11. VSM in-plane hysteresis loops, measured at room temperature, corresponding to $\text{Co}_{100-x}\text{-Cu}_x$ samples after annealing at 270 °C. x is the proportion of Cu on the target surface. (a) $x = 5$ and (b) $x = 20$. The loops corresponding to the initial hard direction for the magnetization (blue square symbols) and the initial easy direction (red circle symbols) are now equal. The solid lines are visual guides, ($\theta_{\text{deposition}} = 55$ deg.).

The dependence of the electrical resistance, R , on temperature for different Co–Cu films is shown in Figure 12. R was measured between two contacts in a direction perpendicular to the longitudinal direction of the nano-sheets. An increase with x of the initial resistance at room temperature, R_0 , was measured: the higher the Cu content, the higher the R_0 . At 450 °C, the values of the resistance at room temperature became almost equal for all of the samples ($R \approx 10\text{--}20 \Omega$). In this Figure 12, relaxation processes are visualized as was expected for amorphous or nano-crystalline materials that were initially out of thermodynamic equilibrium at room temperature [18,19]. These structural relaxation processes were considered as irreversible processes of atoms' diffusion from high energy positions, which are metastable, to other atomic positions with lower energy or even to the final stable crystalline structure with the lowest energy.

Figure 12 shows that R remained approximately constant up to temperatures of ≈ 150 °C; therefore, no indications of structural relaxation were detected from room temperature to this temperature. The structure of the amorphous Co, and those of the amorphous Co matrix with the Cu nanocrystals dispersed in it, was thermally stable up to ≈ 150 °C. From ≈ 150 to 450 °C, R decreased with increasing temperature. For Co and for $x = 5$, there was a change in the slope of the curve with a drop at ≈ 280 °C. This drop was almost imperceptible in the $x = 50$ sample. Therefore, the relaxation processes of the Co samples were affected by the higher or lower Cu content and should also be related to the different nano-morphology of the samples. This suggested somewhat that for $x > 20$, the nano-sheet morphology was not as well defined as it was for $x = 0, 5$ and 10 (in accordance with the simultaneous decrease in H_k). This will be discussed in the next section.

We studied the energy required to cause structural relaxation processes as a function of the Cu content in these Co–Cu films formed by oblique nano-sheets. For this purpose, the activation energy spectra of the atomic processes that took place during annealing were obtained using the Primark's model [48], in the same way as we reported for Co, Co-V and Co-Zn films [18,19]. The annealing temperature, T , was related to the activation energy, E_0 , by the equation $E_0 = (kT/b) (\ln(v_0T/V_s) - a)$, where k is the Boltzmann constant, v_0 is the Debye frequency for single atom jumps (10^{12} s^{-1}) [18,19,49] and V_s is the annealing rate (0.17 K s^{-1}). a and b are fitted parameters (in our case, $a = 2.6$ and $b = 1.03$) on account of the approximations detailed in References [49,50], that is, $(E_0/kT + \ln[(E_0/kT) + 2]) \approx a + (E_0/kT)b$) and taking the interval 0.5–2.5 eV, typical for structural relaxation phenomena in amorphous materials [49]. The activation energy spectrum was calculated using the variation of the resistance with temperature and the equation $p_0 = (-1/R_0)(dR/dT)(dE_0/dT)^{-1}$, where p_0 is the density of activated atoms for each energy (measured in atoms/eV) and R_0 is the value of the resistance in the as-deposited state.

Figure 13 shows the calculations for some of the Co–Cu films. In the curves $p_0(E_0)$, it can be observed: first, the absence of activated states below a threshold energy $E_0 \approx 1.2$ eV. Second, an increasing value of the density of activated atoms for each energy, p_0 , in the energy interval from this threshold to the energy corresponding to the maximum value of p_0 . Third, the existence of two peaks in these spectra whose energies depend on x .

The first peak appeared at $E_0 = 1.61$ eV for Co and $E_0 = 1.62$ eV for $x = 5$ ($E_0 = 1.63$ eV for $x = 10$, not included in the Figure). This first peak broadened for $x = 20$, with a similar value, $E_0 = 1.67$ eV, and finally, it disappeared for $x = 50$, see Figure 13d.

The second peak experienced a continuous linear shift to higher energies as x increased, from 1.85 eV for Co to 2.16 eV for $x = 30$ (not shown in Figure 13). It also broadened as x increased. For $x = 50$ there were no sharp peaks, except for a broad one centered at $E_0 \approx 1.7$ eV.

The evolution of both peaks with x is represented in Figure 14. The first one remained almost constant up to $x = 30$ and disappeared for $x = 50$. The second peak increased linearly with x and also vanished when $x = 50$.

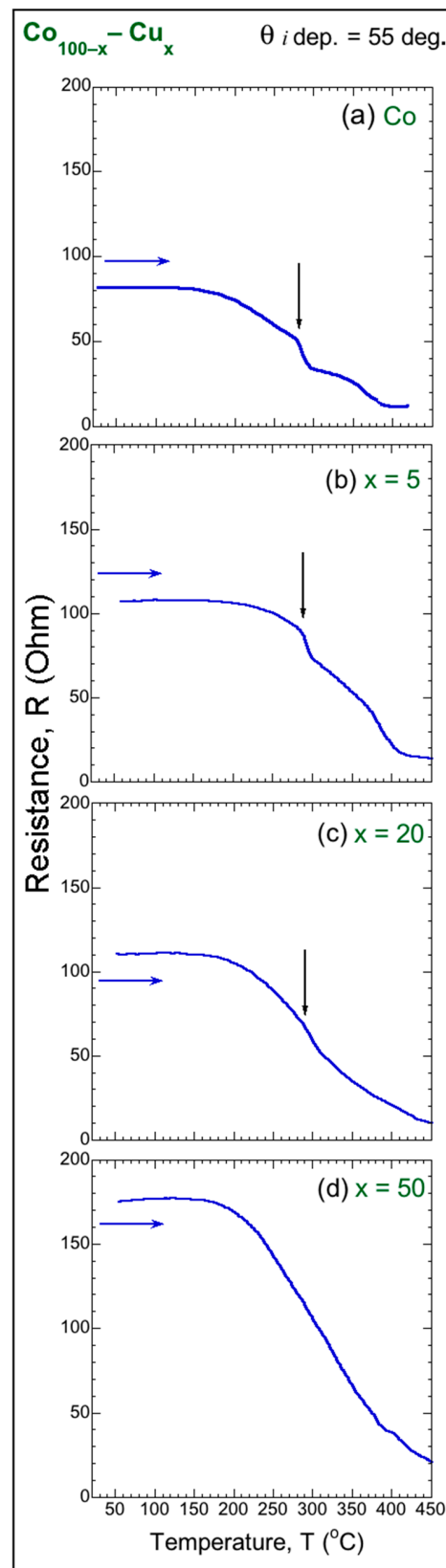


Figure 12. Dependence of the resistance R on the temperature T corresponding to $\text{Co}_{100-x}\text{-Cu}_x$ samples. x is the proportion of Cu on the target surface. (a) Co, (b) $x = 5$, (c) $x = 20$ and (d) $x = 50$. The blue dashed arrows indicate the direction of temperature increase when measuring all of the curves. The black arrows point to the first significant drop in the curves, almost not observed in (d) (see text for an explanation), ($\theta_{i \text{ deposition}} = 55 \text{ deg.}$).

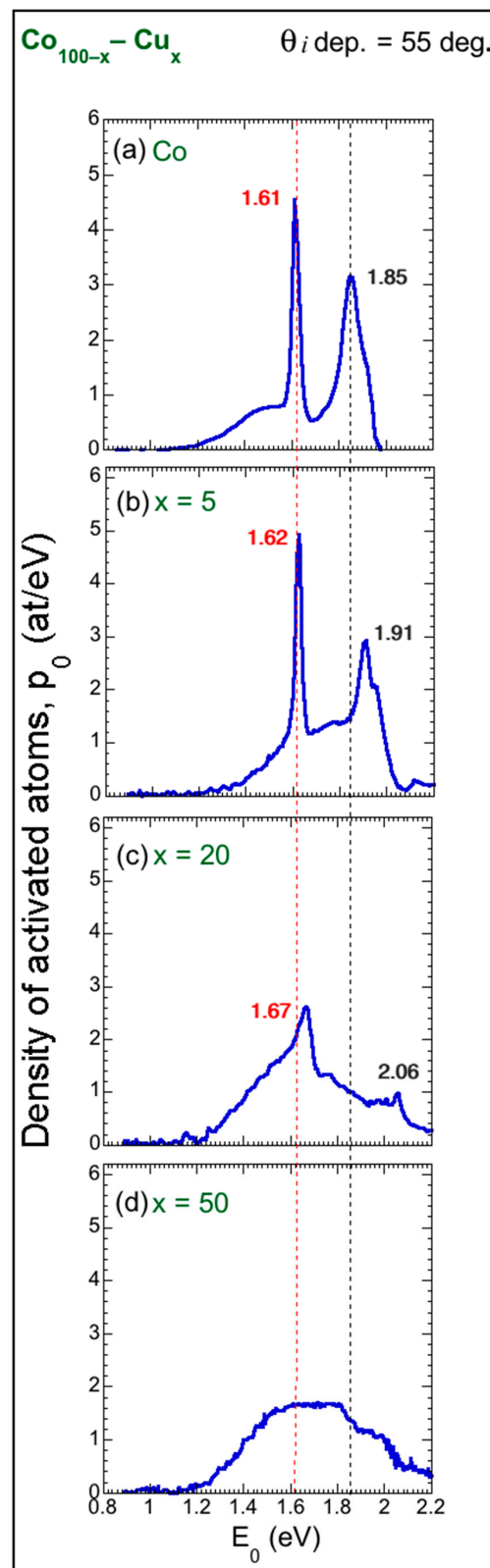


Figure 13. Activation energy spectra of the processes that took place during annealing of $\text{Co}_{100-x}\text{-Cu}_x$ films. x is the proportion of Cu on the target surface. The spectra were obtained from measurements of the dependence of resistance on temperature. (a) Co, (b) $x = 5$, (c) $x = 20$ and (d) $x = 50$. The dashed red line marks the position of the first peak for Co and the black one indicates the position of the second peak for Co. The values of activation energy E_0 for the different peaks and samples are indicated, ($\theta_{i\text{deposition}} = 55 \text{ deg.}$).

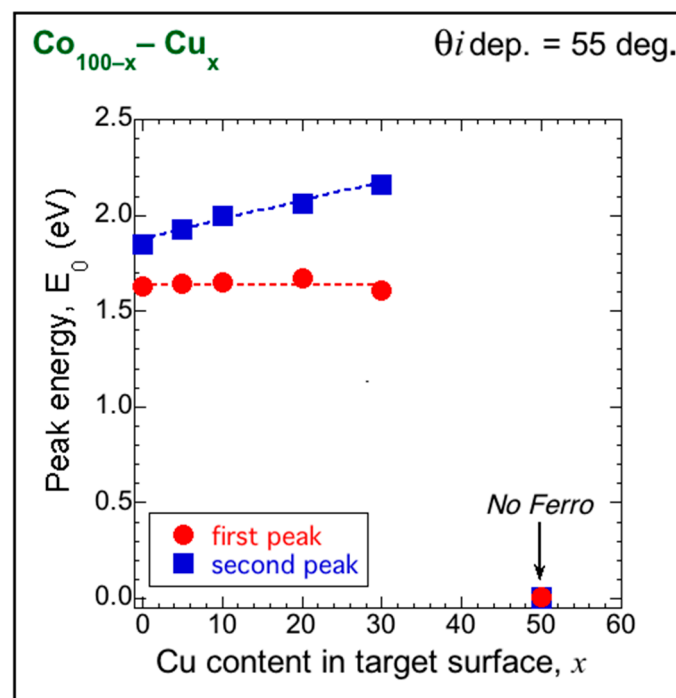


Figure 14. Dependence on the Cu content x of the energy of the two peaks appearing on the activation energy spectra of the $\text{Co}_{100-x}\text{-Cu}_x$ films. They were calculated from the dependence of their resistance with temperature. x is the proportion of Cu in the target surface. The red and blue lines are visual guides. For $x = 50$, the samples are non-ferromagnetic. ($\theta_{\text{deposition}} = 55$ deg.).

3.3. Summary of Main Results and Final Discussion

The main results of this work are as follows:

- (1) The existence of an in-plane uniaxial magnetic anisotropy (UMA) for the obliquely deposited $\text{Co}_{100-x}\text{-Cu}_x$ films (55 deg. films);
- (2) The loss of the UMA after annealing the obliquely deposited $\text{Co}_{100-x}\text{-Cu}_x$ films;
- (3) For the 55 deg. films: The increase of the density of activated atoms for each energy, p_0 , in the energy interval between a threshold energy and the energy of the maximum value of p_0 , as observed in the activation energy spectra of the structural relaxation processes, as well as a presence of two peaks whose energies and widths depended on x . The energy corresponding to the first peak is almost constant for $x = 0$ to 30, whereas the energy of the second peak increases linearly with x ;
- (4) The smaller size of the Cu nano-crystals in the 55 deg. samples with respect to those present in the 0 deg. films;
- (5) The decrease of the coercive field H_c with x for the 55 deg. films, in contrast with the increase of H_c with x for the 0 deg. samples;
- (6) The decrease of the coercive field H_c with the average size d of the Cu grains for the 55 deg. samples, in contrast with the increase of H_c with d for the 0 deg. samples;
- (7) The superparamagnetic character of both 55 deg. and 0 deg. films for $x = 50$.

(1) *The existence of an in-plane uniaxial magnetic anisotropy (UMA) for the obliquely deposited $\text{Co}_{100-x}\text{-Cu}_x$ films, 55 deg. samples.*

From X-ray diffraction, we found that the 55 deg. Co and the Co–Cu films exhibited either an amorphous-like structure or a structure with well-visible Cu crystals whose size, always in the nano-metric range, depended on the Cu content. All of these samples exhibited a clear in-plane uniaxial magnetic anisotropy; thus, we discarded a magneto-crystalline anisotropy as its origin. The magnetic anisotropy could be explained accounting for a special nano-morphology that did not exist in the 0 deg. samples. According to our

previous studies, we deduced that the morphology of both types of samples must have been quite different, despite the similarity in their respective X-ray diffraction measurements.

From our former findings of obliquely deposited Co and Co-rich films [17–19] briefly described above, we knew that the Co nano-sheets were ≈ 3.0 – 5.0 nm thick, ≈ 70 nm wide and ≈ 200 – 300 nm long, with an inter-sheet distance of ≈ 1.0 – 2.5 nm and that they were oriented perpendicular to the incidence plane of the plasma and tilted at an angle ≈ 60 deg. with respect to the substrate plane. These oriented nano-sheets, with similar dimensions and tilt angle, were also observed in oblique deposited Co–V and Co–Zn films [19]. Therefore, we deduced that this nano-morphology was also present in the Co–Cu samples studied in the present work, since we observed here the top surface of nano-sheets. Analogously, we attribute here the origin of the magnetic anisotropy of these Co–Cu films to a shape anisotropy, whose origin lies in the growth, during deposition, of tilted nano-sheets, similar to those described above. Note that for these Co–Cu films, we found the same easy direction for the magnetization as in the previous Co and Co–MT samples (MT = V, Cr, Hf, Zn, Cd . . .) [17,19]. This assumption on the origin of the anisotropy was as well based on the fact that the technique for depositing the Co–Cu films was the same as the one used in our previous works in terms of our special experimental set-up [17–23].

Hence, in accordance with these previous observations, with the X-ray analysis (Figure 6), with the observation of the surface of nano-sheets, revealed as nano-strings oriented perpendicular to the incidence plane of the plasma during deposition (Figure 7) and therefore with the deduction of the presence of tilted nano-sheets, and, we could conclude that, in the case of $\theta_{i_{\text{deposition}}} = 55$ deg., the $\text{Co}_{100-x}\text{--Cu}_x$ films with $x = 0, 5$ and 10 had an amorphous structure or small nano-crystals of Co and Cu with 1 or 2 nm in size and by magnetostatic considerations, the nano-sheets forced the magnetization to be located in the longitudinal direction of the nano-sheets. Note that this fact coincided with both, the almost absence of Cu peaks (nor Co) and the nearly constant value of the anisotropy field, H_k for the three compositions (Figures 6–9). The decrease in the value of H_k for the films with $x = 20$ and 30 was attributed to the growth of the non-magnetic Cu crystals whose size (between ≈ 5 and 11 nm), placement and orientation must have been such that they hindered the alignment of the magnetic moments of Co along the longitudinal direction of the nano-sheets. The presence of textured Cu nano-crystals in the (111) directions, increasing in number and size, probably weakened the nano-sheet structure, thus decreasing the UMA. This misalignment was greater for the more Cu in the samples. The specific location of the Cu atoms could be of importance, not only for the values of H_k , but also for the loss of that UMA observed in the annealed samples: We already demonstrated that the loss of the anisotropic properties after heating the samples was highly dependent on the position of the non-magnetic atoms [19]. Our studies on similar Co–Zn films in the as-deposited state showed that the nano-sheets contained principally Co ($\approx \text{Co}98\%$ – $\text{Zn}2\%$) inside the nano-sheets. In the inter-nano-sheet spaces, a relative proportion $\approx \text{Co}93\%$ – $\text{Zn}7\%$, was measured. Furthermore, a high proportion of Zn was beneath the nano-sheets in the lower region of the films. Since these Co–Cu films behaved similarly to the Co–Zn ones in terms of the presence of UMA in the as-deposited state and the subsequent loss of this UMA after annealing, we can think that the location of the non-magnetic Cu grains must have been similar to the location of the non-magnetic Zn grains in the Co–Zn samples, being segregated from the Co nano-sheet structure. We could also consider that this possible placement of Cu below the Co nano-sheets could be more noticeable the higher the Cu content in the films because, for $x \geq 20$, the Cu grains had an average size much larger than the distance between two consecutive nano-sheets. This hinders the percolation of Co (and even more the formation of nano-sheets), the film being non-magnetic for $x = 50$.

In contrast, the normally deposited Co–Cu films did not exhibit UMA, as these samples did not have a morphology of nano-sheets (as we have shown in Figure 7a). Our PLD 0 deg. Co films also had small nano-crystals (measuring 1 or 2 nm), but they randomly oriented and homogeneously distributed in the film [17,42], and neither nano-sheets nor UMA were observed in these films [17,18]. This magnetic anisotropy was not present in

0 deg. Co–MT films (MT = V, Zn, Cd, Hf, Cu, Cr . . .) [17]. As occurred in the case of the obliquely deposited films, the normally deposited films also lost their ferromagnetism for x between 30 and 50.

(2) *The loss of the UMA after annealing the obliquely deposited $\text{Co}_{100-x}\text{Cu}_x$ films.*

The loss of the UMA in all of the Co–Cu films (shown in Figure 11 for some of them) could be ascribed to the transformation of their nano-sheet morphology. Certainly, as we showed in Ref. [18], the nano-sheets present in as-deposited Co samples endured a significant transformation after annealing at 270 °C; although somehow still showing a pattern of oblique Co nano-sheets, the separation between them decreased and the nano-sheets merged. A coalescence-like process occurred, the nano-sheets of Co approached each other, coming into the contact between them [18]. This nano-morphological process of the extinction of oriented nano-sheets was simultaneous to the disappearance of the uniaxial anisotropic behavior of several physical parameters, including the magnetic one. Furthermore, a similar process of disappearance of the nano-sheets in annealed Co–Zn films allowed us to attribute the loss of the UMA to this loss of the tilted nano-sheets as well [19]. Thus, we could assume here a similar process for the Co–Cu films. In conclusion, the most important fact with respect to the anisotropic properties loss at this temperature was the loss of the nano-sheet morphology after their coalescence process.

(3) *For the 55 deg. films: The increase of the density of activated atoms for each energy, p_0 , in the energy interval between a threshold energy and the energy of the maximum value of p_0 , as observed in the activation energy spectra of the structural relaxation processes, as well as a presence of two peaks whose energies and widths depended on x . The energy corresponding to the first peak is almost constant for $x = 0$ to 30, whereas the energy of the second peak increases linearly with x .*

The differences in these structural relaxation phenomena among the different films reflected in the $p_0(E_0)$ curves shown in Figure 13 could be associated with their nano-sheets morphology, and this dependence on x could also be understood as a directional relaxation. The continuous increase in p_0 corresponding to the energy interval from the threshold energy $E_0 \approx 1.2$ eV to just before the first peak appearance must have corresponded to the transformations of the nano-sheets probably present in the samples.

As we previously demonstrated [18], in the absence of nano-sheets (in normally deposited films) this continuous increase in p_0 did not exist. It was reasonable to think that these transformations were probably initiated in the space among the nano-sheets, corresponding to relaxations within the metastable amorphous state of atoms, or clusters of atoms located in this space, giving rise to coalescence between nano-sheets. This produced contact between the nano-sheets, and thus they deteriorated. We could deduce from Figure 13 that the larger x was, the earlier this process of nano-sheets coalescence started. Certainly, comparing the curves in this energy range, $E_0 \approx 1.2$ and 1.56 eV, it was observed that samples with $x \geq 20$ exhibited a greater increase in the p_0 values than samples with $x \leq 10$. In accordance with previous findings in similar Co–Zn films [19], this fact could also be favored by the presumable localization of the larger Cu grains beneath the nano-sheets, acting as a “buffer layer” and easing the contact among the nano-sheets.

It was also shown in Figure 13 that the energy corresponding to the first peak remained almost constant. This peak could be attributed to the relaxation of amorphous Co located in the inner parts of the nano-sheets, or of Co surrounded by some small Cu nano-crystals (undetectable by our X-ray measurements), i.e., relaxation processes without Co (or Cu) growth. The decrease of E_0 from 1.61 to 0 eV from $x = 30$ to 50 could be principally linked to the weakness of the nano-sheets due to the presence of larger Cu grains and to the presence of isolated Co clusters; in these cases, the relaxation phenomena were not as directional but were more isotropic. This fact was supported by the width of this first peak, see again Figure 13. The more Cu content, the wider the peak was (the limit was the spectrum corresponding to $x = 50$, there was no peak).

The second peak in the spectra, visible at higher energies compared to the energies corresponding to the first one, was due to the crystallization processes of Co (and to a lesser extent of Cu). The displacement of the peak to higher energies as x increased was caused by

the greater difficulty of percolation and growth of the Co grains as the Cu content increased. There was a “limit” for the $x = 50$ sample in which the as-deposited amorphous Co could not easily grow and crystallize, with the small nano-crystals remaining isolated from their neighbors, in spite of the energy given to the system upon annealing. This displacement of this second peak was not directly associated with the nano-sheets but was essentially to the Cu content since it is believed that, for those high energies, the nano-sheets no longer existed in these Co–Cu samples, in accordance with our previous results on Co and Co–Zn films [18,19].

(4) *The smaller size of the Cu nano-crystals in the 55 deg. samples with respect to those present in the 0 deg. films.*

The greater ease of nano-crystal growth must be related to the kinetics of nucleation and the films deposition–growth process. In the 0 deg. samples, nano-crystal growth and grain coalescence during films deposition was favored because the nucleation centers were randomly distributed, without shadowing effects. This also promoted not only their growth in samples with smaller x ($x = 0, 5$ and 10) but also their larger size. Note also that this larger size was measured in pure Cu films, not only in Co–Cu films.

(5) and (6) The decrease of the coercive field H_c with x for the 55 deg. films, in contrast with the increase of H_c with x for the 0 deg. samples and the decrease of H_c with the average size d of the Cu grains for the 55 deg. samples, in contrast with the increase of H_c with d for the 0 deg. samples.

This must also be linked to the different nano-morphologies generated during the growth of the samples. In both cases (55 and 0 deg. samples), when Cu crystals were recognizable, the qualitative evolution of H_c with x was similar to the evolution of H_c with the d . These results are shown together as a summary in Figure 15 to ease the comparison. In this Figure, and for $x = 0, 5$ and 10 in the 55 deg. samples, the grain size were assumed to be almost zero, as seen in Figure 15c, since we only measured a small peak corresponding to Cu(200) planes for $x = 10$, with nano-crystals around 1–2 nm in size.

In the 55 deg. pure Co sample, the inter-nano-sheet spaces, ≈ 2 nm [18] could act as voids or “non-magnetic inclusions”, hindering the nucleation and displacements of the magnetic domain walls. This was because when a wall contains such inclusions, the wall energy is reduced because its area decreases; thus, the wall tends to stay anchored, requiring the application of higher magnetic fields to move the walls [51] (p. 302). As the proportion and size of Cu grains increased, assuming that they were mainly located on the bottom surfaces of the samples, it would decrease the volume occupied by the nano-sheets; consequently, the coercive field H_c progressively decreased, see Figure 15a–c.

In contrast, in the absence of inclined nano-sheet morphology in the 0 deg. films, H_c increased with both x and d , as seen in Figure 15d,e. In this case, the immiscibility of Cu in Co played a crucial role as a structural singularity for the movement of magnetic domain walls, as the walls tend to become attached to the non-magnetic particles. These walls were in an amorphous-nanocrystalline Co matrix with randomly distributed non-magnetic Cu clusters increasing in size as Cu content increased, Figure 15f. These grains increased the number of domain wall pinning sites. Consequently, the coercivity H_c increased substantially.

(7) *The superparamagnetic character of both 55 and 0 deg. films for $x = 50$.*

This superparamagnetic behavior appeared due to the nanometer size of the individual Co clusters, each of which behaved as an isolated magnetic entity with a high net magnetization [44]. This magnetic isolation was enhanced by the increase of the size of Cu clusters that nulled the exchange magnetic interaction among the Co entities. These non-ferromagnetic Co–Cu films are under further study and the results will be published elsewhere.

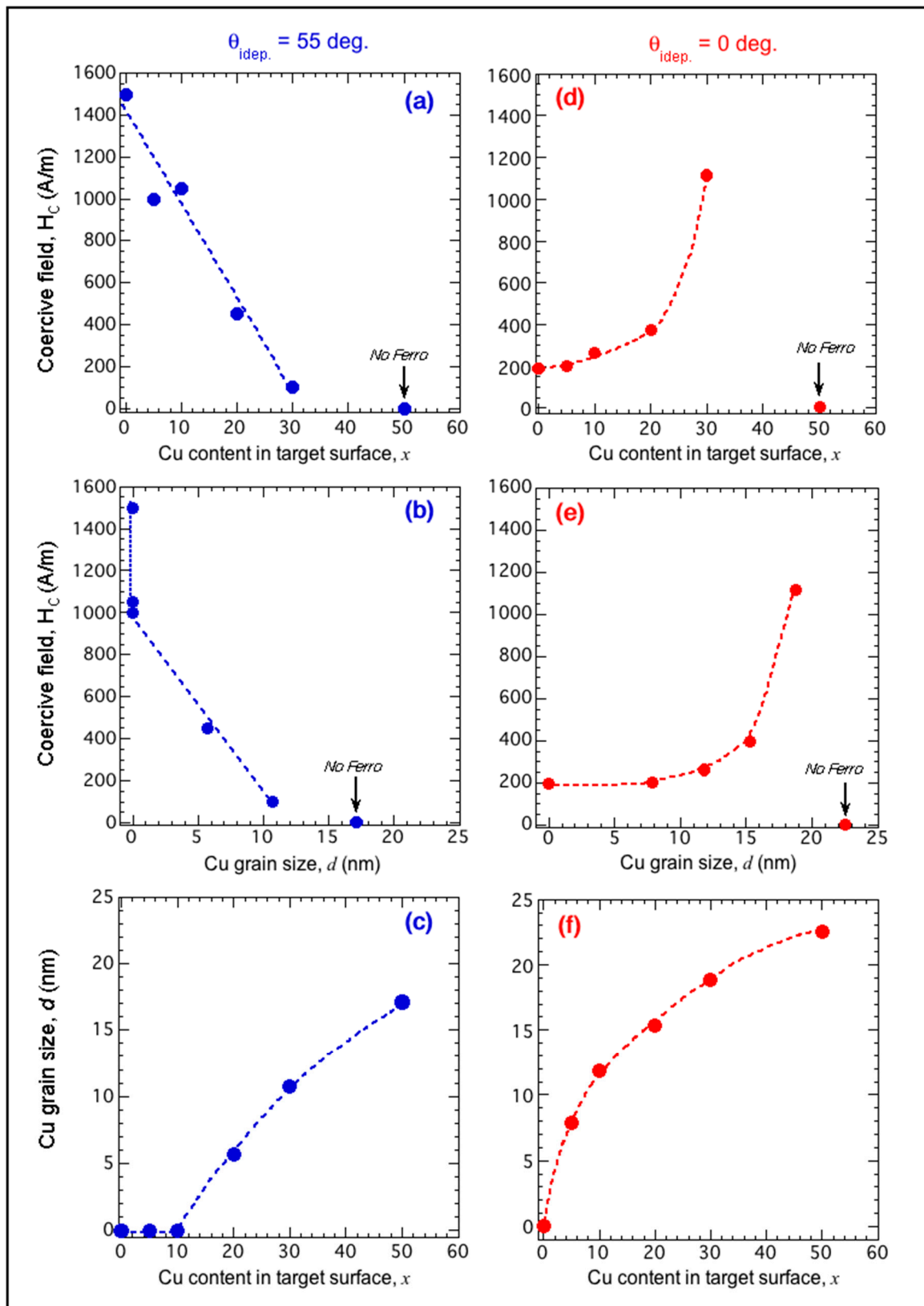


Figure 15. (a–c) For $\theta_{\text{ideposition}} = 55 \text{ deg.}$ (a) dependence of the coercive field H_c with x . x is the proportion of Cu on the target's surface.; (b) evolution of H_c with the Cu average grain size, d ; (c) dependence of d with x . (d–f) For $\theta_{\text{ideposition}} = 0 \text{ deg.}$, (d) dependence of H_c with x ; (e) evolution of H_c with d ; (f) dependence of d with x . The dotted lines are visual guides.

4. Conclusions

Thin films of $\text{Co}_{100-x}\text{-Cu}_x$ were grown by pulsed laser deposition. Their magnetic properties were tailored by controlling their nano-morphology, their nano-structure and their composition through changes in growth conditions. Specifically we studied the influence of (i) the normal or oblique angle of incidence of the plasma during deposition and (ii) Cu content.

A special morphology of slanted nano-sheets with cylindrical symmetry was generated only during the growth of the films by oblique incidence ($\theta_i = 55$ deg.), producing in-plane uniaxial magnetic anisotropy; the anisotropy field remained constant at $\approx 35 \text{ kAm}^{-1}$ for the $x = 0, 5$, and 10 films, while it decreased when x increased to 20 and 30. This constant uniaxial anisotropy field was present as long as neither Cu nor Co nano-crystals grew larger than 1–2 nm. When the Cu crystallites were present, with average sizes larger than $\approx 5\text{--}6$ nm and up to 11 nm, the anisotropy decreased, being $\approx 23\%$ lower. With increasing Cu content and nano-crystal size, the easy coercive field decreased from 1500 ($x = 0$) to 100 Am^{-1} ($x = 30$). The inter-nano-sheet spaces could act as “non-magnetic inclusions” and made difficult the nucleation and movement of magnetic domain walls. As the proportion and size of Cu grains increased, the volume occupied by the weakened nano-sheets would decrease and H_c significantly decreased.

Activation energy spectra of the temperature-induced structural relaxations processes were obtained for the 55 deg. samples. For all spectra, it was observed that: (1) an absence of activated states below a threshold energy, $E_0 \approx 1.2$ eV; (2) a continuous increase in p_0 corresponding to the energy interval from that threshold energy to before the first peak is reached; (3) two peaks in these activation energy spectra, peaks whose energies were x -dependent. The continuous increase of p_0 in the $p_0(E_0)$ curves could be attributed to transformations of the nano-morphology, transformations that were considered to start in the inter-nano-sheet spaces and to correspond to relaxations of atoms located in these spaces. This resulted in a continued weakness of the initial nano-morphology. Specifically, in samples with $x \geq 20$, there was an increase in p_0 for energies between 1.2 and 1.56 eV with respect to the curves corresponding to samples $x \leq 10$; i.e., the larger the x , the earlier this nano-sheet coalescence process started. The first peak could be principally associated to relaxations of the atoms located in the inner parts of the nano-sheets. The second peak was due to the crystallization of Co (and to a lesser extent Cu), and shifted to higher energy values on increasing x . This shift had its origin in the greater difficulty of Co grains to percolate and grow as there were more and larger Cu nano-crystals.

The normally deposited films were magnetically isotropic in their plane and magnetically soft. The size of the Cu crystallites increased with x , from ≈ 8 nm ($x = 5$) to ≈ 19 nm ($x = 30$). The coercive field increased from 200 ($x = 0$) to 1100 Am^{-1} ($x = 30$). The small grains ($\approx 1\text{--}2$ nm) of Co, initially ferromagnetically coupled, suffered a weakness in their exchange interaction due to the presence of non-magnetic Cu grains, especially when their size was larger than 15 nm. These grains increased the number of domain wall pinning sites and the coercivity H_c increased remarkably.

In both cases of oblique deposition and normal deposition, superparamagnetic behavior was observed for $x = 50$.

Author Contributions: Conceptualization, C.F., V.M., J.V.; investigation, C.F., V.M., J.V.; methodology, C.F., V.M., J.V.; formal analysis, C.F., V.M., J.V.; writing—original draft preparation, C.F.; writing—review and editing, C.F., V.M., J.V.; visualization, C.F. All authors have read and agreed to the published version of the manuscript.

Funding: This research received no external funding.

Acknowledgments: Financial support from the Public University of Navarre is acknowledged. The authors have not received funds from any other Institution.

Conflicts of Interest: The authors declare no conflict of interest.

References

1. Liu, J.P.; Fullerton, E.; Gutfleisch, O.; Sellmyer, D.J. *Nanoscale Magnetic Materials and Applications*; Springer: New York, NY, USA, 2006.
2. Johnson, M.T.; Bloemen, P.J.H.; den Broeder, F.J.A.; De Vries, J.J. Magnetic anisotropy in metallic multilayers. *Rep. Prog. Phys.* **2001**, *59*, 1409–1458. [[CrossRef](#)]
3. Scheunert, G.; Heinonen, O.; Hardeman, R.; Lapicki, A.; Gubbins, M.; Bowman, R.M. A review of high magnetic moment thin films for microscale and nanotechnology applications. *Appl. Phys. Rev.* **2016**, *3*, 011301. [[CrossRef](#)]
4. Hämäläinen, S.; Madami, M.; Qin, H.; Gubbiotti, G.; Van Dijken, S. Control of spin-wave transmission by a programmable domain wall. *Nat. Commun.* **2018**, *9*, 4853. [[CrossRef](#)]
5. Song, T.; Cai, X.; Tu, M.W.-Y.; Zhang, X.; Huang, B.; Wilson, N.P.; Seyler, K.L.; Zhu, L.; Taniguchi, T.; Watanabe, K.; et al. Giant tunneling magnetoresistance in spin-filter van der Waals heterostructures. *Science* **2018**, *360*, 1214–1218. [[CrossRef](#)]
6. Dai, S.; He, Y.; Huang, H.; Zhang, H.; Zhang, J.; Peng, Y.; Bai, F. Electrodeposited CoCu/Cu meta-conductor with suppressed skin effect for next generation radio frequency electronics. *J. Alloys Compd.* **2019**, *778*, 156–162. [[CrossRef](#)]
7. Sander, D.; Valenzuela, S.O.; Makarov, D.; Marrows, C.H.; Fullerton, E.E.; Fischer, P.; Mccord, J.; Vavassori, P.; Mangin, S.; Pirro, P.; et al. The 2017 Magnetism Roadmap. *J. Phys. D Appl. Phys.* **2017**, *50*, 363001. [[CrossRef](#)]
8. Hawkeye, M.M.; Brett, M.J. Glancing angle deposition: Fabrication, properties, and applications of micro- and nanostructured thin films. *J. Vac. Sci. Technol. A* **2007**, *25*, 1317. [[CrossRef](#)]
9. Ohring, M. *Materials Science of Thin Films Deposition and Structure*, 2nd ed.; Elsevier Inc.: Amsterdam, The Netherlands, 2002.
10. Hida, R.; Falub, C.V.; Perraudau, S.; Morin, C.; Favier, S.; Mazel, Y.; Saghi, Z.; Michel, J.-P. Nanolaminated FeCoB/FeCo and FeCoB/NiFe soft magnetic thin films with tailored magnetic properties deposited by magnetron sputtering. *J. Magn. Magn. Mater.* **2018**, *453*, 211–219. [[CrossRef](#)]
11. Mendil, J.; Trassin, M.; Bu, Q.; Schaab, J.; Baumgartner, M.; Murer, C.; Dao, P.T.; Vijayakumar, J.; Bracher, D.; Bouillet, C.; et al. Magnetic properties and domain structure of ultrathin yttrium iron garnet/Pt bilayers. *Phys. Rev. Mater.* **2019**, *3*, 034403. [[CrossRef](#)]
12. Gupta, P.; Akhila, K.J.; Srihari, V.; Svec, P.; Kane, S.R.; Rai, S.K.; Ganguli, T. On the origin of magnetic anisotropy of FeCo(Nb)B alloy thin films: A thermal annealing study. *J. Magn. Magn. Mater.* **2019**, *480*, 64–72. [[CrossRef](#)]
13. Shena, J.; Gaib, Z.; Kirschner, J. Growth and magnetism of metallic thin films and multilayers by pulsed-laser deposition. *Surf. Sci. Rep.* **2004**, *52*, 163–218. [[CrossRef](#)]
14. Van Kranenburg, H.; Lodder, C. Tailoring growth and local composition by oblique-incidence deposition: A review and new experimental data. *Mater. Sci. Eng. R Rep.* **1994**, *11*, 295–354. [[CrossRef](#)]
15. Mattox, D.M. *Handbook of Physical Vapor Deposition (PVD) Processing*; Elsevier: Amsterdam, The Netherlands, 2010.
16. Krebs, H.-U.; Bremert, O. Pulsed laser deposition of thin metallic alloys. *Appl. Phys. Lett.* **1993**, *62*, 2341–2343. [[CrossRef](#)]
17. Favieres, C.; Vergara, J.; Magen, C.; Ibarra, M.; Madurga, V. Building oriented nano-sheets in thin films of Co–MT (MT = V, Cr, Cu, Zn, Cd, Hf) and the generation and enhancement of their magnetic anisotropy. *J. Alloys Compd.* **2016**, *664*, 695–706. [[CrossRef](#)]
18. Vergara, J.; Favieres, C.; Magén, C.; De Teresa, J.M.; Ibarra, M.R.; Madurga, V. Structurally Oriented Nano-Sheets in Co Thin Films: Changing Their Anisotropic Physical Properties by Thermally-Induced Relaxation. *Materials* **2017**, *10*, 1390. [[CrossRef](#)]
19. Favieres, C.; Vergara, J.; Magén, C.; Ibarra, M.R.; Madurga, V. Vanadium trapped by oblique nano-sheets to preserve the anisotropy in Co-V thin films at high temperatures. *J. Alloys Compd.* **2021**, submitted for publication.
20. Madurga, V.; Vergara, J.; Favieres, C. Magnetic domain structures and nano-string morphology of laser off-normal deposited amorphous cobalt films with controlled magnetic anisotropy. *J. Magn. Magn. Mater.* **2004**, *272–276*, 1681–1683. [[CrossRef](#)]
21. Madurga, V.; Favieres, C.; Vergara, J. Growth and sculpting of Co nano-strings on Si micro-cantilevers: Magneto-mechanical properties. *Nanotechnology* **2010**, *21*, 095702. [[CrossRef](#)] [[PubMed](#)]
22. Madurga, V.; Vergara, J.; Favieres, C. Generating and measuring the anisotropic elastic behaviour of Co thin films with oriented surface nano-strings on micro-cantilevers. *Nanoscale Res. Lett.* **2011**, *6*, 325. [[CrossRef](#)]
23. Favieres, C.; Vergara, J.; Madurga, V. Tailoring the anisotropic physical properties of thin films for sensors applications by controlling their oblique nano-sheets morphology. *J. Mater. Sci. Nanomater.* **2018**, *2*, 2.
24. Liu, L.; Qi, L.; Han, R.; Zhang, H.; Wang, Y.; Sun, H. Growth mechanism and magnetic properties of dendritic nanostructure prepared by pulse electrodeposition. *J. Alloys Compd.* **2017**, *694*, 1239–1245. [[CrossRef](#)]
25. Dhara, S.; Chowdhury, R.R.; Bandyopadhyay, B. Disorder in Co-Cu granular alloys studied by ⁵⁹Co NMR. *J. Magn. Magn. Mater.* **2019**, *471*, 355–358. [[CrossRef](#)]
26. Zhang, H.; Jia, W.; Sun, H.; Zhang, X.; Guo, L.; Hu, J. Electrochemical preparation and magnetic properties of Co–Cu nanometric granular alloy films. *Bull. Mater. Sci.* **2019**, *42*, 103. [[CrossRef](#)]
27. Zhukov, A.; Mino, J.; Del Val, J.; Varga, R.; Martinez, G.; Baibich, M.; Ipatov, M.; Churyukanova, M.; Zhukova, V. GMR effect and Kondo-like behaviour in Co-Cu microwires. *J. Alloys Compd.* **2017**, *695*, 976–980. [[CrossRef](#)]
28. Esmaeili, A.; Kashi, M.A.; Ramazani, A.; Montazer, A. Tailoring magnetic properties in arrays of pulse-electrodeposited Co nanowires: The role of Cu additive. *J. Magn. Magn. Mater.* **2016**, *397*, 64–72. [[CrossRef](#)]
29. Cho, C.-W.; Park, S.; Bae, J.; Park, S. Effect of a Cu buffer layer on the structural, chemical and magnetic properties of Co layers. *J. Magn. Magn. Mater.* **2014**, *354*, 54–57. [[CrossRef](#)]
30. Zhang, Q.-F.; Zheng, H.-F.; Wang, L.-S.; Su, A.-M.; Liu, X.; Xie, J.; Chen, Y.; Peng, D.-L. Influence of surface and interface modification on the electrical transport behaviors in Co@Cu nanocomposite films. *Magn. Magn. Mater.* **2018**, *460*, 34–40. [[CrossRef](#)]

31. Stücker, M.; Teichert, C.; Matković, A.; Krenn, H.; Weissitsch, L.; Wurster, S.; Pippin, R.; Bachmaier, A. On the magnetic nanostructure of a Co-Cu alloy processed by high-pressure torsion. *J. Sci. Adv. Mater. Dev.* **2021**, *6*, 33–41. [[CrossRef](#)]
32. Zhang, J.; Peng, Y.; Ma, H.; Zhang, S.; Hu, Y.; Zeng, X.; Deng, X.; Guan, C.; Chen, R.; Hu, Y.; et al. Magnetotransport Mechanism of Individual Nanostructures via Direct Magnetoresistance Measurement in situ SEM. *ACS Appl. Mater. Interfaces* **2020**, *12*, 39798–39806. [[CrossRef](#)]
33. Liu, Y.; Liu, Y.; Shi, H.; Wang, M.; Cheng, S.H.-S.; Bian, H.; Kamruzzaman, W.; Cao, L.; Chung, C.; Lu, Z. Cobalt-copper layered double hydroxide nanosheets as high performance bifunctional catalysts for rechargeable lithium-air batteries. *J. Alloys Compd.* **2016**, *688*, 380–387. [[CrossRef](#)]
34. Reyes, D.; Biziere, N.; Warot-Fonrose, B.; Wade, T.; Gatel, C. Magnetic Configurations in Co/Cu Multilayered Nanowires: Evidence of Structural and Magnetic Interplay. *Nano Lett.* **2016**, *16*, 1230–1236. [[CrossRef](#)]
35. Shpetnyi, I.; Kondrakhova, D.; Vorobiov, S.; Scheibe, B.; Grebinaha, V.; Derecha, D.; Gorobets, Y.; Protsenko, I. The structural-phase state and magnetoresistive properties of thin film alloys obtained by co-evaporated Cu and Co. *J. Magn. Magn. Mater.* **2019**, *474*, 624–631. [[CrossRef](#)]
36. Jogschies, L.; Klaas, D.; Kruppe, R.; Rittinger, J.; Taptimthong, P.; Wienecke, A.; Rissing, L.; Wurz, M.C. Recent Developments of Magnetoresistive Sensors for Industrial Applications. *Sensors* **2015**, *15*, 28665–28689. [[CrossRef](#)] [[PubMed](#)]
37. Sugime, H.; D’Arsié, L.; Esconjauregui, S.; Zhong, G.; Wu, X.; Hildebrandt, E.; Sezen, H.; Amati, M.; Gregoratti, L.; Weatherup, R.S.; et al. Low temperature growth of fully covered single-layer graphene using a CoCu catalyst. *Nanoscale* **2017**, *9*, 14467–14475. [[CrossRef](#)]
38. Filiz, B.C.; Figen, A.K.; Pişkin, S. The remarkable role of metal promoters on the catalytic activity of Co-Cu based nanoparticles for boosting hydrogen evolution: Ammonia borane hydrolysis. *Appl. Catal. B Environ.* **2018**, *238*, 365–380. [[CrossRef](#)]
39. Lowndes, D.H.; Geohegan, D.B.; Puretzky, A.A.; Norton, D.P.; Rouleau, C.M. Synthesis of Novel Thin-Film Materials by Pulsed Laser Deposition. *Science* **1996**, *273*, 898–903. [[CrossRef](#)] [[PubMed](#)]
40. Hiroshima, Y.; Ishiguro, T.; Urata, I.; Makita, H.; Ohta, H.; Tohogi, M.; Ichinose, Y. Fundamental properties in the formation of Co, Ni, and Pt metal thin films using pulsed laser deposition. *J. Appl. Phys.* **1996**, *79*, 3572–3577. [[CrossRef](#)]
41. Horcas, I.; Fernández, R.; Gómez-Rodríguez, J.M.; Colchero, J.; Gómez-Herrero, J.; Baro, A.M. WSXM: A software for scanning probe microscopy and a tool for nanotechnology. *Rev. Sci. Instrum.* **2007**, *78*, 013705. [[CrossRef](#)]
42. Cullity, B.D.; Stock, S.R. *Elements of X-ray Diffraction*, 3rd. ed.; Pearson Education International, Inc.: Prentice Hall, NJ, USA, 2001; p. 170.
43. Favieres, C.; Madurga, V. Determination of the thickness of pulsed laser deposited cylindrical Co films by their magnetoelastic effects. *J. Appl. Phys.* **2004**, *96*, 1850–1856. [[CrossRef](#)]
44. Bean, P.; Livingston, J.D. Superparamagnetism. *J. Appl. Phys. Suppl.* **1959**, *30*, 120S–129S. [[CrossRef](#)]
45. Dahlberg, E.D.; Riggs, K.; Prinz, G.A. Magnetotransport: An ideal probe of anisotropy energies in epitaxial films. *J. Appl. Phys.* **1988**, *63*, 4270–4275. [[CrossRef](#)]
46. Favieres, C.; Madurga, V. Magnetoelastic properties of laser-ablated non-crystalline Co cylindrical films. *J. Non-Cryst. Solids* **2001**, *287*, 390–395. [[CrossRef](#)]
47. Favieres, C.; Vergara, J.; Madurga, V. Charged magnetic domain walls as observed in nanostructured thin films: Dependence on both film thickness and anisotropy. *J. Phys. Condens. Matter* **2013**, *25*, 066002. [[CrossRef](#)]
48. Primak, W. Kinetics of Processes Distributed in Activation Energy. *Phys. Rev.* **1955**, *100*, 1677–1689. [[CrossRef](#)]
49. Baricco, M.; Allia, P.; Vinai, F.; Riontino, G. Structural relaxation in FeNiCrPB amorphous alloys by joint isothermal and tempering measurements of the electrical resistivity. *J. Mater. Sci.* **1988**, *23*, 4287–4294. [[CrossRef](#)]
50. Hernando, A.; Nielsen, O.V.; Madurga, V. Relaxation processes and pure shear stress creep in a metallic glass ribbon of composition $(\text{Fe}_{0.05}\text{Co}_{0.95})_{75}\text{Si}_{15}\text{B}_{10}$. *J. Mater. Sci.* **1985**, *20*, 2093–2102. [[CrossRef](#)]
51. Cullity, D.; Graham, C.D. *Introduction to Magnetic Materials*, 2nd. ed.; John Wiley & Sons Inc.: Hoboken, NJ, USA, 2009.